IRAQI JOURNAL OF APPLIED PHYSICS
Vol. 22, No. 1, January-March 2026, pp. 109-120

Enhancing P3HT-Based Organic Solar Cells via $CsGeI_2Br$ Perovskite Interlayer Integration

Hayder M.M. Al-duhaidahawi [1]
Asghar Asgari [2]
Burak Y. Kadem [3*]

[1,2] Faculty of Physics, University of Tabriz, Tabriz, IRAN
[1,2] Research Institute for Applied Physics and Astronomy, University of Tabriz, Tabriz, IRAN
[3] College of Science, Al-Karkh University of Science, Baghdad, IRAQ
*Corresponding author: drburakkadem@gmail.com

In this study, the impact of incorporating an intrinsic perovskite layer ($CsGeI_2Br$) on the performance of P3HT-based organic solar cells was investigated using numerical simulation. A multi-layer device structure (PCBM/C60/P3HT/Cu_2O) was modeled with and without the insertion of the perovskite layer between the C60 and P3HT layers. Various physical parameters were optimized, including the perovskite thickness, bandgap, electron affinity, defect density, and effective density of states. The results indicate that the inclusion of the perovskite layer enhances photon absorption, facilitates charge carrier separation, and reduces recombination losses-resulting in a significant improvement in power conversion efficiency (PCE). The optimized structure achieved a PCE of 33.46%, compared to 26.9% for the device without the perovskite layer. These findings highlight the potential of lead-free perovskite materials in advancing high-performance, environmentally sustainable organic photovoltaics.

Keywords: SCAPS-1D; P3HT:PCBM; Perovskite solar cells; Intrinsic layer
Received: 25 May 2025; Revised: 3 August; Accepted: 10 August; Published: 1 January 2026

1. Introduction

Solar energy has experienced significant improvements while also encountering critical challenges, such as climate change and environmental concerns, through directly converting sunlight into electricity via photovoltaic (PV) cells [1]. The latter generally consists of a combination of N-type and P-type semiconductors [2]. Generally, the majority of PV technologies are silicon-based due to the material's abundance and superior mechanical and thermal stability. Despite their dominance in the market, silicon-based PV cells remain financially inaccessible to low-income populations due to the high manufacturing costs. Organic solar cells (OSCs) are lightweight, flexible, and solution-processable photovoltaics with great potential for integration into wearable textiles, smart electronics, and sustainable architecture [3-8]. Poly (3-hexylthiophene) (P3HT), which represents the electron donor and the C60 and its derivatives, such as [6,6]-phenylC61- butyric acid methyl ester (PCBM), acting as the electron acceptor, are widely used in organic solar cells [9]. On the other hand, perovskite solar cells (PSC) offer a promising alternative, as they fulfill both cost-effectiveness and high-efficiency requirements, making them a scalable solution to meet the energy demands of low-income communities. Perovskites represent a diverse class of compounds with the general formula ABX_3 , where A is an organic or inorganic cation, B is a divalent metal ion, and X is a halide anion. Perovskite solar cells (PSCs) have rapidly emerged as a promising photovoltaic technology, achieving significant progress, with power conversion efficiencies (PCE) reaching up to 25% within just a few years [10]. These materials offer several advantages, including cost-effectiveness, high efficiency, thin-film deposition, a straightforward fabrication process, tunable energy bandgaps, and excellent electrical and optical properties. However, the majority of perovskite solar cells (PSCs) still rely on toxic elements such as lead (Pb) and corrosive organic cations like methylammonium (MA) and formamidinium (FA) [11-17], primarily due to their high efficiency. In response to these concerns, only a limited number of researchers have explored the development of homojunction PSCs (single absorber layer) that eliminate toxic elements and reduce corrosivity. Some notable examples include $Cs_2GeSnCl_6$ [18], $Cs_2GeSnBr_6$ [19], and $CsSnBr_3$ [20]. Despite these advancements, limited research has been dedicated to $CsGeI_xBr_{3-x}$ perovskite materials, which offer tunable bandgaps based on iodine composition and exhibit high thermal stability up to 350°C [21]. Additionally, since germanium (Ge) belongs to the same group in the periodic table as lead (Pb), germanium-based halide perovskites have garnered significant attention [22]. Because $CsGeI_2Br$ is a relatively less explored mixed-halide germanium perovskite, its specific energy levels can vary depending on factors such as synthesis methods, halide composition, processing conditions, and the influence

of the organic cation, particularly when compared to lead-based analogues. Chiara and co-authors [23] noted that the incorporation of germanium in place of lead provides an additional degree of freedom for tuning the electronic properties beyond simple halide substitution. The bandgap has been suggested within the range of 1.5–1.6 eV (see table 1). This may correspond to a valence band energy close to 5.1–5.3 eV and a conduction band around 3.6–3.7 eV. These energy levels suggest a highly favorable energy level alignment with P3HT and PCBM, as illustrated in Scheme 1 for charge separation and transportation to their respective electrodes. In the current study, organic solar cells with the structure (PCBM/C60/P3HT/Cu2O) are simulated with and without using CsGeI2Br intrinsic perovskite layer between C60 and P3HT layers. Here, the term 'intrinsic' refers to an intrinsic-like (compensated) semiconductor, where donor and acceptor concentrations are equal, effectively mimicking intrinsic behavior in simulation (ND = NA). The main goal is to improve the OSC performance, achieving PCE acceding 30%. Several parameters were examined such as the perovskite thickness, the CB and VB effective density of states, perovskite E_g and E_A as well as the total density of defect states. To the best of the author knowledge, this is the first attempt to employ lead-free perovskite such as $CsGeI_2Br$ inserted between P3HT and C60 layers which can act as an interfacial energy level bridge. To date, nearly all perovskite-inserted hybrid structures have used Lead-based perovskites or perovskite active layers rather than interlayers. Unlike Pb-based interlayers, this material is environmentally benign and structurally compatible. Few reports (and sometimes none, depending on the specific composition) have studied $CsGeI_2Br$ as an interfacial layer in an organic heterojunction in combination with P3HT/C60, targeting energy alignment in that stack.

2. Device Model and Simulation Parameters

The simulation consists of PCBM/C60/P3HT/Cu_2O solar device under AM 1.5 G 1sun and 100 mW/cm^2 illumination, where Buckminsterfullerene (C60) was used as the electron acceptor [24], poly(3-hexylthiophene) (P3HT) as the electron donor [25] and lead free perovskite ($CsGeI_2Br$) as intrisic layer. The configuration of this solar cell is illustrated in scheme (1).

SCAPS 1D software uses Poisson Eq. (1), continuity Eqs. (2) and (3) and carrier transport Eqs. (4) and (5) for electrons and holes to obtain the current density-voltage (J-V) characteristics:

$$\Delta\varepsilon\Delta\phi = = q(p - n + N_D^+ - N_A^-) \quad (1)$$

For electrons:

$$\Delta J_n = q(R - G) + q\frac{\partial n}{\partial t} \quad (2)$$

For holes:

$$\Delta J_p = q(R - G) + q\frac{\partial p}{\partial t} \quad (3)$$

For electrons:

$$J_n = D_n\frac{dn}{dx} + \mu_n n\frac{d\phi}{dx} \quad (4)$$

For holes:

$$J_p = D_p\frac{dp}{dx} + \mu_p p\frac{d\phi}{dx} \quad (5)$$

where: ε is the dielectric constant, N_D and N_A are the donor and acceptor densities, respectively, p and n are the free holes and free electrons, ϕ is the electrostatic potential, J_n and J_p are the current densities for the electrons and the holes, respectively, R and G are the recombination and generation rates, respectively, and μ_n and μ_p are the electron and hole mobility, respectively. Note that SCAPS-1D solves the coupled Poisson and continuity equations under the assumption of a one-dimensional geometry [29]. This simplification neglects lateral (2D/3D) inhomogeneity such as grain boundaries, edge effects, non-uniform illumination, and shunt paths that can occur in real devices. Additionally, SCAPS assumes ideal planar interfaces, uniform material properties within each layer, and does not clearly account for lateral carrier diffusion or recombination at grain boundaries. While these assumptions are standard and appropriate for modeling the vertical transport and J–V characteristics in layered devices, they may introduce deviations when comparing to real-world cells with complex morphologies [29]. The simulated parameters of the materials used in this study are illustrated in Table 1. All initial values were chosen based on experimental and/or simulation work as cited in the table for the best value in these references.

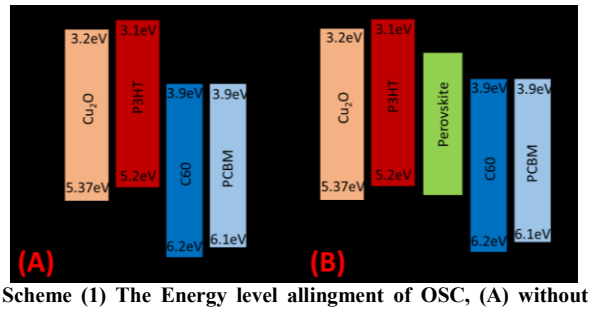

Scheme (1) The Energy level allingment of OSC, (A) without perovskite layer, and (B) with perovskite layer. Cu_2O energy levels are cited from [26], P3HT and PCBM are cited from [27] and C60 energy level are cited from [28]

The photovoltaic properties in the form of current density-voltage (J-V) dependence are usually used to calculate the fill factor (FF) and the power PCE according to the following equations [32]:

$$PCE\ (\%) = \frac{J_{max}V_{max}}{P_{in}} \quad (6)$$

$$FF = \frac{J_{max}V_{max}}{J_{sc}\ V_{oc}} \quad (7)$$

where J_{sc} is the short-circuit current density (mA/cm^2), V_{oc} is the open-circuit voltage (V), P_{in} is the incident light power and J_{max} (mA/cm^2) and V_{max} (V) are the current density and voltage at the point of maximum power output in the J-V curves, respectively

3. Results and Discussions

3.1. Symmetric absorber thickness with and without intrinsic perovskite layer

The effects of using an intrinsic perovskite layer between P3HT and C60 organic layer are examined. Fig. (1A) illustrates the energy band alignment of the OSC without a perovskite layer. The perovskite layer thickness, as well as the organic layers, have symmetric thickness in this section, and all the results in this section are based only on the effect of using the intrinsic perovskite layer. This alignment shows good band bending at the interface between P3HT and the C60 layer. However, introducing the perovskite layer (see Fig. 1B) has resulted in a graded band bending structure. Electron- hole separation can be improved by designing bandgap- graded profiles in absorbers [33].

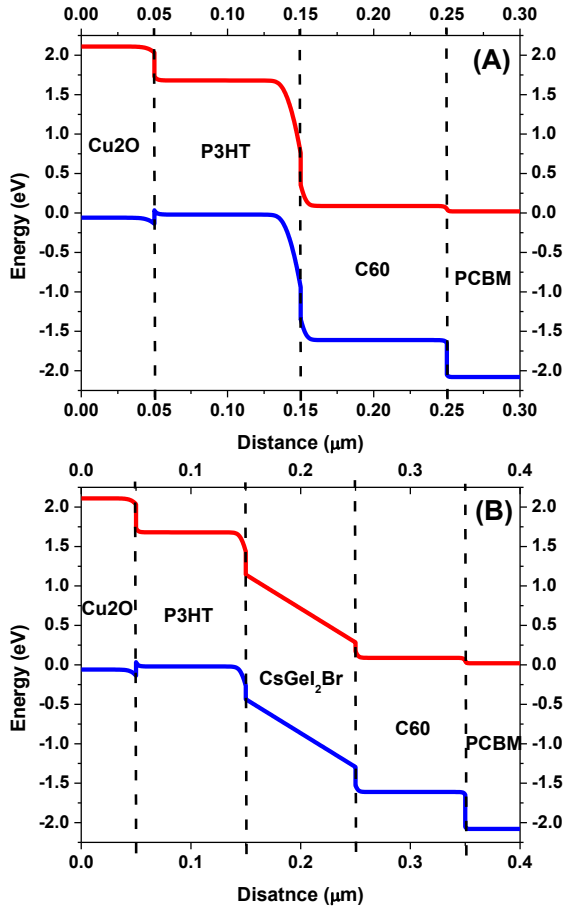

Fig. (1) Energy band alignment of OSC (A) without and (B) with perovskite layer

The incorporation of a perovskite layer can enhance current density by improving photon absorption, facilitating charge carrier separation, and generating an electric field gradient. This gradient supports charge extraction while reducing recombination losses, thereby increasing charge collection efficiency. The resulting electric field, known as the built-in potential (V_{bi}), can be determined using a Schottky-Mott plot, where the extrapolated intersection of the straight line with the voltage axis (as shown in Fig. 2A) represents V_{bi}. A notable increase in V_{bi} from 1.2 V to 1.3 V is observed after incorporating the intrinsic perovskite layer. Furthermore, the depletion width (W) generally expands with increasing reverse bias, following the equation [34]:

$$W = \sqrt{\frac{2\varepsilon_o\varepsilon_r(V_{bi} - V)}{qN_A}} \qquad (8)$$

where ε_o is the permittivity of free space, ε_r is the relative permittivity. Additionally, variations in capacitance indicate a significant impact on interface properties when a perovskite layer is introduced between P3HT and C60

This modification can influence electron extraction at the interface, playing a crucial role in determining overall solar cell performance [35]. The depletion width has three main areas as shown in Fig. (2B). In a solar cell, the depletion width **(**W**)** refers to the region where charge carriers are depleted, leaving behind an electric field that assists in charge separation. Under reverse bias, this depletion width expands, improving charge separation and reducing recombination losses. On the other hand, at forward bias the depletion width decreases (area 3) especially close to the V_{oc} value.

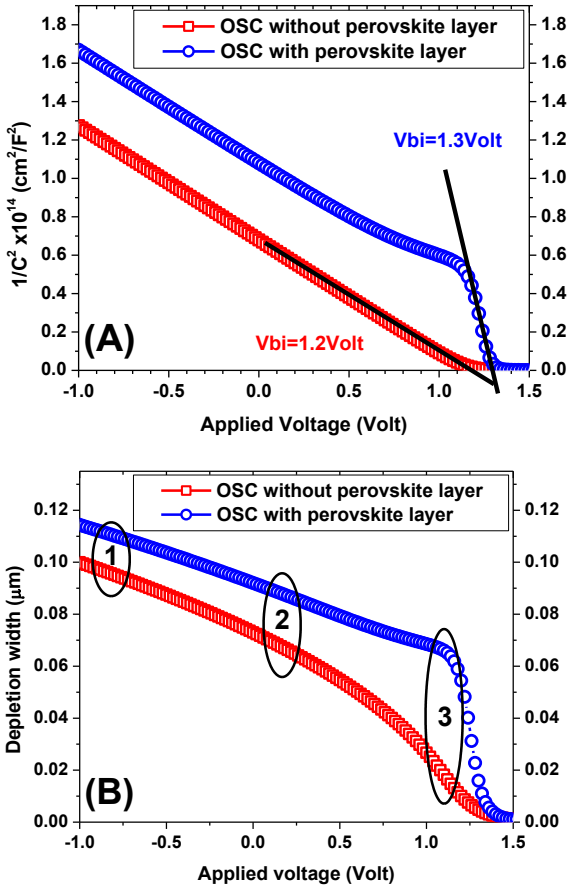

Fig. (2) (A) Schottky-Mott plot, and (B) Depletion width vs applied voltage

The solar cell performance of the OSC with and without using an intrinsic perovskite layer is simulated, results are shown in Fig. (3A) where the IV curves demonstrate obvious enhancement in the solar cell characteristics; the solar cell parameters are illustrated in table (2). Open circuit voltage has exhibited almost similar values with and without using the perovskite layer. While, short circuit current density increases from 19.37 mA.cm^{-2} to 23.24 mA.cm^{-2} for the devices without and with perovskite layer, respectively. This enhancement is due to the higher absorption characteristics confirmed by quantum efficiency curve shown in Fig. (3B). This increase is attributed to the perovskite band gap which is in the range of 15-1.6eV.

The OSC without perovskite layer has demonstrated wide spectral response, especially close to the absorber band gap as shown in Fig. (3C), whereas, the introduction of perovskite layer enhances this response to lower energies. Also, the incorporation of a perovskite layer enhances J_{sc} by improving photon absorption, facilitating charge carrier separation, and generating an electric field gradient. This results in better FF and therefore high PCE as shown in table (2).

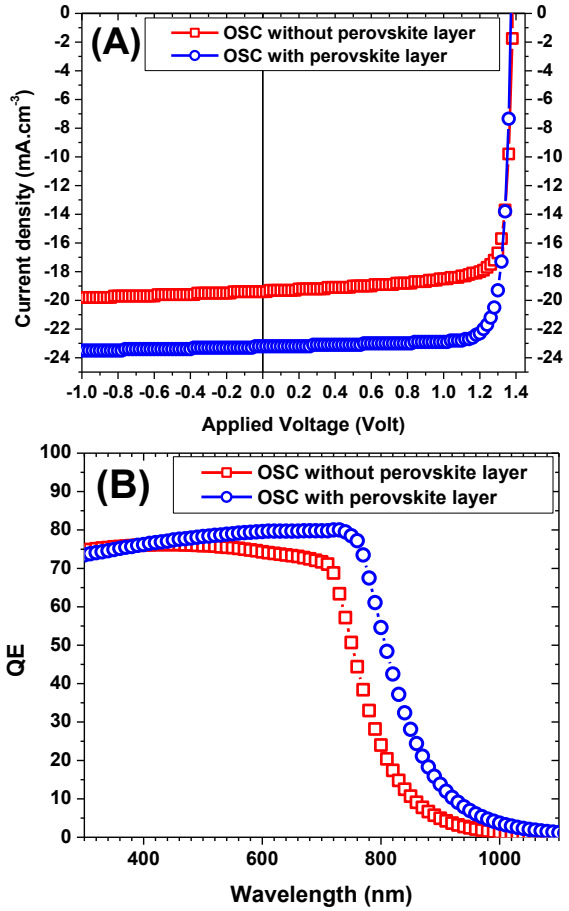

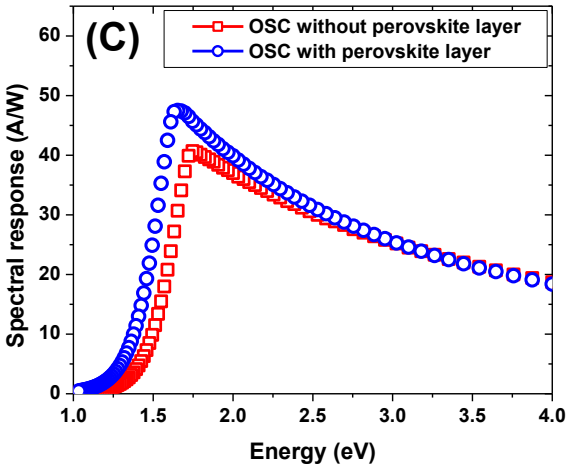

Fig. (3) (A) IV characteristics, (B) Quantum efficiency, and (C) Spectral response for the OSC with and without perovskite layer

Table (2) Solar cell parameters for the OSC with and without perovskite layer

Device	V_{oc} (Volt)	J_{sc} (mA.cm^{-2})	FF	PCE
OSC without perovskite	1.38	19.37	82.4	22.1
OSC with perovskite	1.37	23.24	84.3	26.9

3.2. Different perovskite thickness

In this section, different perovskite thicknesses ranging from 50nm to 500nm were examined to investigate their effects on the solar cell performance and results are demonstrated in Fig. (4A and B).

Typically, the maximum light intensity within the absorbing layer is positioned at a specific distance from the electrode, determined by the refractive index and layer thickness. As a result, the electric field distribution shifts the absorption region further from the interface to an area with higher field strength, enhancing J_{sc} [36]. As the intrinsic layer thickness increases up to 500 nm, J_{sc} improves due to enhanced light absorption and the corresponding generation of more electron-hole pairs (see Fig. 4A). However, charge carrier collection at the respective electrodes declines as the transport distance for photogenerated carriers increases in a thicker absorber layer, leading to a reduction in V_{oc} [37]. The slight decrease in V_{oc} (from 1.38 V to 1.323 V) with increasing thickness (see Fig. 4A) is attributed to the rise in dark saturation current (J_o), which results from increased charge carrier recombination [31,38], This relationship can be further explained by the equation linking V_{oc} to the photogenerated current and dark saturation current [39]:

$$V_{oc} = \frac{kT}{q} \ln\left(\frac{J_{sc}}{J_o} + 1\right) \qquad (9)$$

The highest power conversion efficiency (PCE) of 31% is achieved at a 500 nm thickness, with J_{sc}=28 mA/cm², V_{oc}=1.34 V, and a fill factor (FF) of 83.65%. FF experiences a slight reduction with increasing

thickness form 50 to 500nm due to increased series resistance (R_s). The FF is primarily influenced by shunt resistance (R_{sh}), which governs leakage current, and R_s, which is mainly attributed to contact resistance between the active layer and electrodes [40]. These resistances can hinder exciton dissociation, leading to higher charge carrier recombination [41], which directly impacts FF [42]. FF has exhibited the values in the range of 83.65-84.4% for all samples.

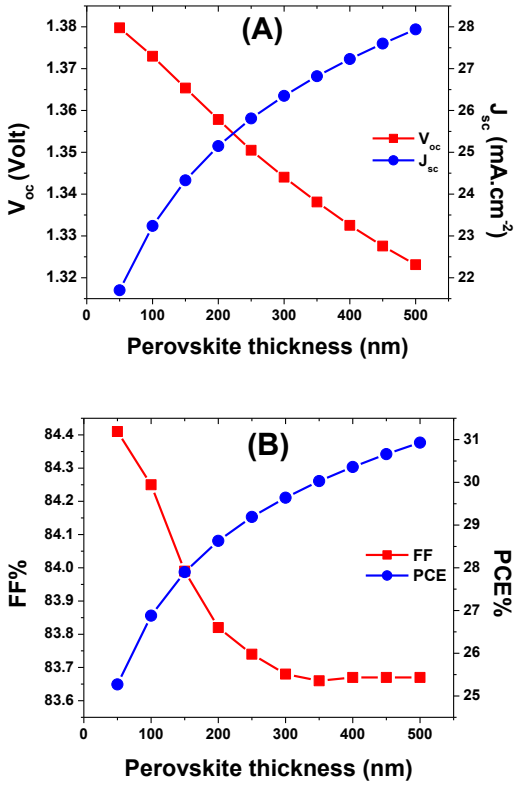

Fig. (4) (A) Voc and Jsc, and (B) FF and PCE, for OSC with different perovskite thicknesses

3.3. Different perovskite band gap (Eg)

The energy bandgap (E_g) plays a crucial role in solar cell performance, as it directly determines the range of light wavelengths that can be absorbed and converted into electrical energy [43]. A well-optimized bandgap allows for efficient photon absorption, maximizing charge carrier generation and overall device efficiency. One of the most attractive aspects of perovskites for photovoltaics is the capability to adjust their energy band gap by simple compositional exchange [43]. The perovskite semiconducting materials utilized in high-performing PSCs typically have energy band gaps between 1.48 eV and 1.62 eV, because the perovskite's lower bandgap (1.5–1.6 eV) contributes to enhanced absorption in the near-IR, boosting J_{sc} and spectral response at longer wavelengths [44,45].

In this section, band gaps in the range from 1.5-1.58 eV are examined as shown in Fig. (5). As the bandgap (E_g) increases, the short-circuit current density (J_{sc}) exhibits a noticeable decline, decreasing from 31.5 mA/cm² at E_g=1.5eV to 28.3 mA/cm² at E_g=1.58eV, as shown in Fig. (5A). This energy band increase results in lower absorption properties and, therefore, less contribution in charge generation. Moreover, increasing E_g influences several key parameters, including the Fermi level position and the alignment of the conduction and valence bands. Consequently, the open-circuit voltage (V_{oc}) is affected by changes in E_g, following the relation $\Delta V_{oc}=E_g/qV_{oc}$ [46]. The relationship between fill factor (FF), PCE, and E_g is illustrated in Fig. (5B). The observed decrease in FF with increasing E_g is likely due to an increase in recombination losses [47]. The highest PCE at E_g=1.5eV is primarily attributed to the combined enhancement in FF and J_{sc} [48]. Generally, reducing the bandgap of the absorber material significantly improves the photovoltaic performance of perovskite-based solar cells by enhancing PCE, FF, and J_{sc}.

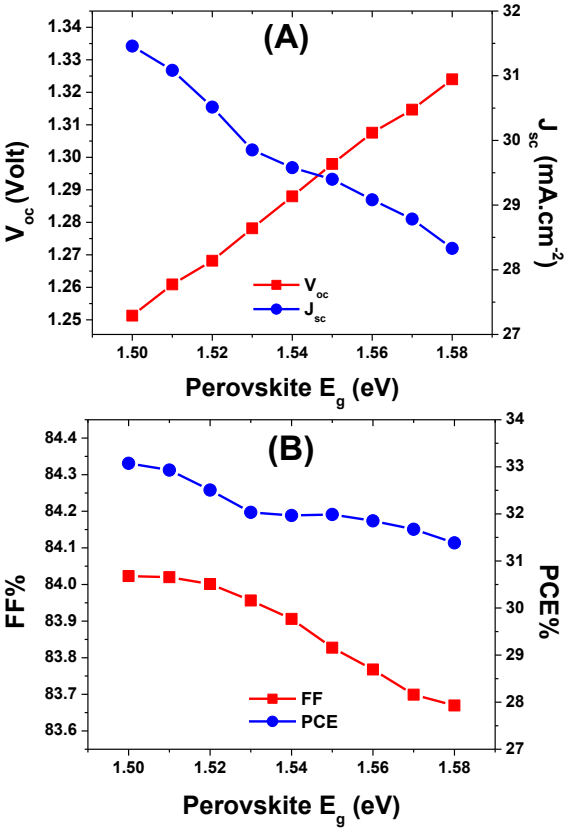

Fig. (5) (A) V_{oc} and J_{sc}, and (B) FF and PCE, for OSC with different perovskite band gap

3.4. Different perovskite Electron affinity (EA)

To evaluate the performance of solar cells, the effect of varying electron affinity (EA) is analyzed. Ding et al [49] explored modifications in chemical composition to specifically adjust electron affinity and bandgap, optimizing device performance parameters. They fine-tuned the band offset by altering key

parameters such as bandgap and electron affinity to enhance overall efficiency. Effective interface engineering is crucial for ensuring the selective extraction of the majority carriers while blocking the minority carriers. An optimal interface should facilitate efficient majority carrier transport while preventing minority carrier recombination. Additionally, variations in bandgap and electron affinity can lead to the formation of cliff or spike structures at the interface [50]. At low electron affinity (3.5eV), spikes are presented at the interfaces Cu_2O/P3HT and P3HT/Perovskite as shown in Fig. (6A). These spikes prevent holes from injected into the absorber layer and reduce recombination [49]. On the other side, high band offset is observed for both conduction and valance bands.

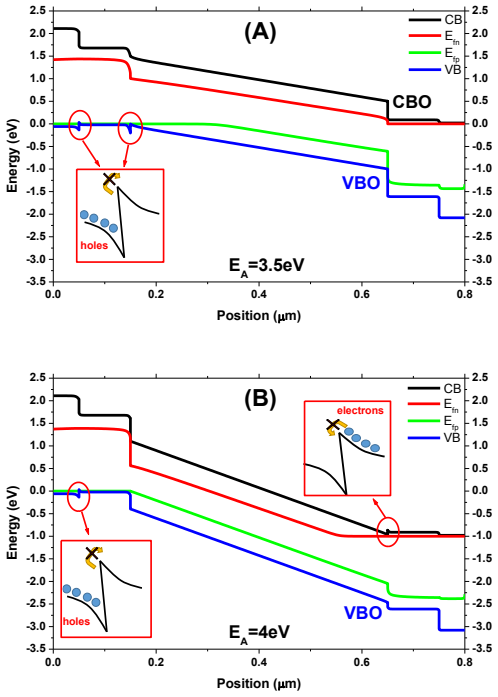

Fig. (6) Energy band alignment with different electron affinity (A) 3.5eV and (B) 4eV

At lower electron affinity values (EA = 3.5 eV), the valence band offsets at the Cu_2O/P3HT and P3HT/perovskite interfaces give rise to noticeable spikes in the valence band. These energetic barriers can hinder the extraction of photogenerated holes from the perovskite absorber into the adjacent hole transport layers. A moderate valence band spike can be advantageous, as it helps suppress the backflow of holes and reduces interfacial recombination by discouraging the accumulation of minority carriers at the interface. However, if the barrier becomes too pronounced exceeding approximately 0.4-0.5 eV it can significantly impede hole extraction, ultimately lowering the fill factor and photocurrent. In contrast, at higher electron affinity (EA=4 eV), as illustrated in Fig. (6B), a prominent spike emerges in the conduction band at the C60/perovskite interface. This conduction band spike acts as a selective barrier to electron transport, effectively preventing photogenerated electrons from diffusing back into the perovskite layer. As a result, recombination between electrons accumulating on the C60 side and holes within the perovskite is strongly suppressed [49]. In addition to reducing recombination, the conduction band spike enhances carrier selectivity, promoting efficient electron collection at the cathode while simultaneously repelling holes. Together, these effects improve charge separation and extraction dynamics, which in turn enhance FF and contribute to higher PCE. Fig. (7) shows the solar cell parameters as a function of different electron affinity values ranging from 3.5 eV to 4 eV. No obvious change in the device V_{oc} and J_{sc} is observed with increasing electron affinity, however, FF exhibited an increase from 84.5% with EA of 3.5eV to 86.6% with EA of 4, this is due to the reduction in the device recombination at higher electron affinity value. As a results, the PCE has increased as shown in Fig. (8B) from about 30.7% to about 32.6%. Therefore, optimizing the EA level is essential for better solar cell performance.

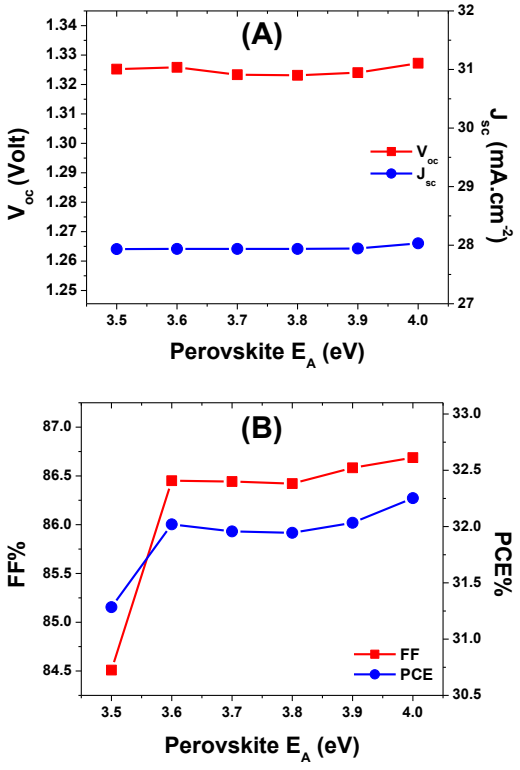

Fig. (7) (A) V_{oc} and J_{sc}, and (B) FF and PCE, for OSC with different perovskite EA

3.5. Different perovskite total defect density of state

The performance of perovskite solar cells is highly influenced by the defect density within the absorber layer and at the interfaces; lower defect densities lead to improved efficiency, as confirmed by several simulation and experimental studies [51-53.]. Recombination through defects is a major loss mechanism for almost all solar cells [54]. Defects have a significant impact on carrier mobility, carrier lifetime, and recombination rates. In addition, intrinsic defects play a key role in setting the doping limits of a material. Therefore, a thorough understanding of defect properties is essential for optimizing solar cell performance [55]. In this section, increasing the defect density of states results in decreasing all the device performance as shown in Fig. (8A and B). Higher density of defects results in lower J_{sc} as more recombination occurs.

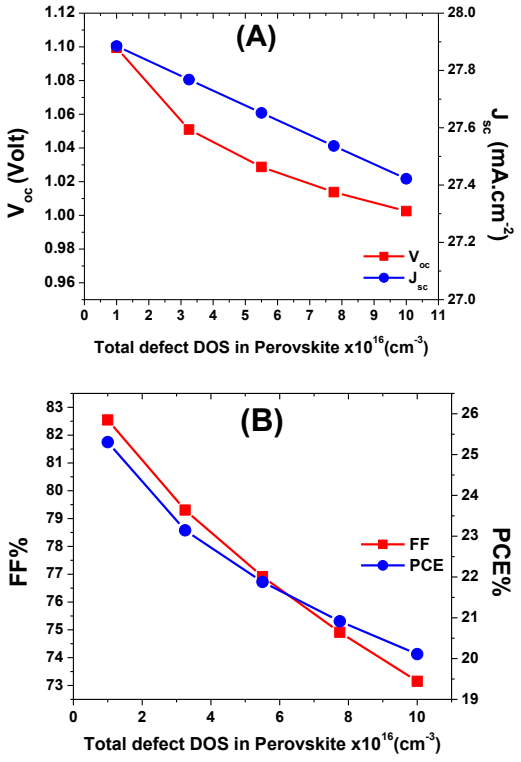

Fig. (8) (A) V_{oc} and J_{sc}, and (B) FF and PCE, for OSC with different DOS in the perovskite

A defect energy level located at 0.6 eV below the conduction band (EC) is present in the absorber layer which corresponds to a relatively deep trap state within the bandgap [56]. These deeper energy levels typically possess high ionization energies and serve as efficient non-radiative recombination centers. By capturing charge carriers, they shorten carrier lifetimes, diminish the open-circuit voltage (V_{oc}), and ultimately constrain overall device performance [57]. Figure (9) illustrates the dependence of perovskite solar cell performance parameters on the absorber's defect density of states. The effect of varying total defect density from 10^{16} to 10^{17} cm^{-3} was analyzed to evaluate the impact on device performance. As shown, the open-circuit voltage (V_{oc}) decreases from 1.1 V at a defect density of 10^{16} cm^{-3} to 1.01 V at 10^{17} cm^{-3}, indicating a strong dependency of V_{oc} on defect density. Similarly, the short-circuit current density (J_{sc}) slightly drops from 27.85 mA/cm² to 27.4 mA/cm² over the same defect density range. The fill factor (FF), which is influenced by both V_{oc} and recombination processes in the depletion region [58], follows a similar trend. It declines from 82.6% at 10^{16} cm^{-3} to 74.3% at 10^{17} cm^{-3}. According to the relation $PCE=V_{oc}\times J_{sc}\times FF$, the power conversion efficiency (PCE) is directly affected by these three output parameters. The highest PCE of 25.4% is achieved at the lowest defect density of 10^{16} cm^{-3}.

3.6. Different perovskite CB and VB effective DOS

In a solar cell under illumination, the open-circuit voltage (V_{oc}) is related to the splitting of the quasi-Fermi levels for electrons and holes, E_{Fn} and E_{Fp} [59]:

$$qV_{oc} = E_{Fn} - E_{Fp} = kT\ln\left(\frac{np}{n_o p_o}\right) \quad (10)$$

$$qV_{oc} = E_g + kT\ln\left(\frac{np}{N_C N_V}\right) \quad (11)$$

where q is the elementary charge, n, p are the concentrations and n_o, p_o the equilibrium concentrations of electrons and holes. While N_C and N_V are the effective densities of states in the conduction and valence band, respectively [60]. Thus, this is a strong argument in favor of low densities of states in materials for high V_{oc} and efficient photovoltaics

From Fig. (9) with CB and VB effective DOS, respectively, V_{oc} decreases with increasing effective DOS, while Js_c remains largely unaffected. This is because the effective DOS primarily influences recombination dynamics rather than the generation of carriers under illumination.

Under short-circuit conditions, the quasi-Fermi level splitting is minimal, leading to low recombination rates and efficient carrier extraction. As a result, changes in the effective DOS have little impact on the number of photogenerated carriers that are collected. Furthermore, increasing the effective DOS on both CB and VB results in decreasing FF; the latter is a function of recombination as shown in Fig. (10). A competition between recombination and extraction of charges that principally determines the dependence of the photocurrent on bias, and hence the FF [61], As a result, PCE reduces with increasing DOS.

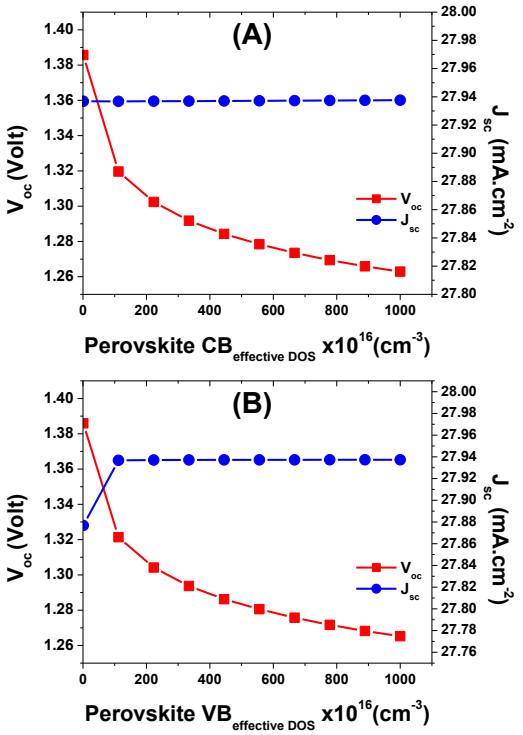

Fig. (9) V_{oc} and J_{sc}, for different effective DOS in the (A) CB and (B) VB of the perovskite

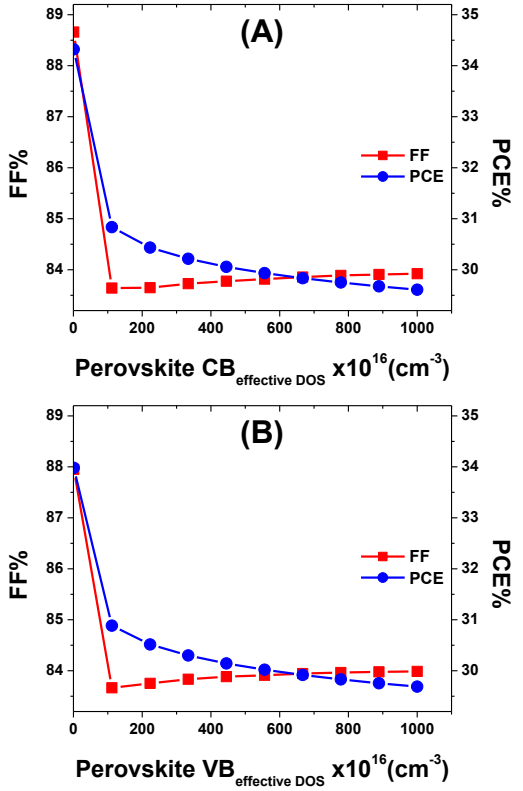

Fig. (10) FF and PCE, for different effective DOS in the (A) CB and (B) VB of the perovskite

3.7. The best device based on the optimum parameters:

The optimum parameters from the previous results were collected to fabricate the best device and simulate its performance and illustrated in table (3). The data presented in Table 3 was performed using a sequential parametric approach in SCAPS-1D. For each key parameter (thickness, band gap, electron affinity, …), we varied it over a relevant range while keeping other parameters at baseline values. After identifying the higher simulated PCE, this parameter was fixed before moving to the next optimization.

The current–voltage (I-V) characteristics and external quantum efficiency (EQE) spectrum of the optimized device are presented in Fig. (11). Through the sequential optimization of the layer parameters, the simulated performance improved markedly. Among all the adjustments, tuning the band gap and increasing the absorber thickness had the most pronounced impact on the power conversion efficiency (PCE), primarily by enhancing light absorption and balancing the photocurrent (J_{sc}) and open-circuit voltage (V_{oc}). Refining the electron affinity further improved the alignment between layers, enabling more effective carrier extraction. Additionally, reducing the trap density helped suppress recombination losses, which contributed to a higher fill factor. Together, these improvements increased the PCE from 26.9% to 33.46%, highlighting the importance of carefully coordinated parameter optimization. The optimized device achieved an open-circuit voltage of 1.39 V, representing a slight increase over the initial configuration shown in table (4). The short-circuit current density (J_{sc}) also rose to 27.9 mA.cm^{-2}, surpassing the initial device performance. Furthermore, the fill factor improved by approximately 2%, reaching 86.48% with the optimized parameters.

Table (4) OCS performance with perovskite layer in the initial and optimum parameters

Device	V_{oc} (V)	J_{sc} (mA/cm^2)	FF	PCE
OSC with perovskite (Initial)	1.37	23.24	84.3	26.90
OSC with perovskite (optimum)	1.39	27.90	86.48	33.46

While the simulated results demonstrate promising performance, the experimental device presents several challenges. In particular, the controlled deposition of high-quality $CsGeI_2Br$ thin films between organic layers like P3HT and C60 requires careful optimization of solvent systems, deposition conditions, and interfacial engineering. Furthermore, maintaining low defect densities and stable energy-level alignment remains a critical obstacle that will need to be addressed in future experimental studies.

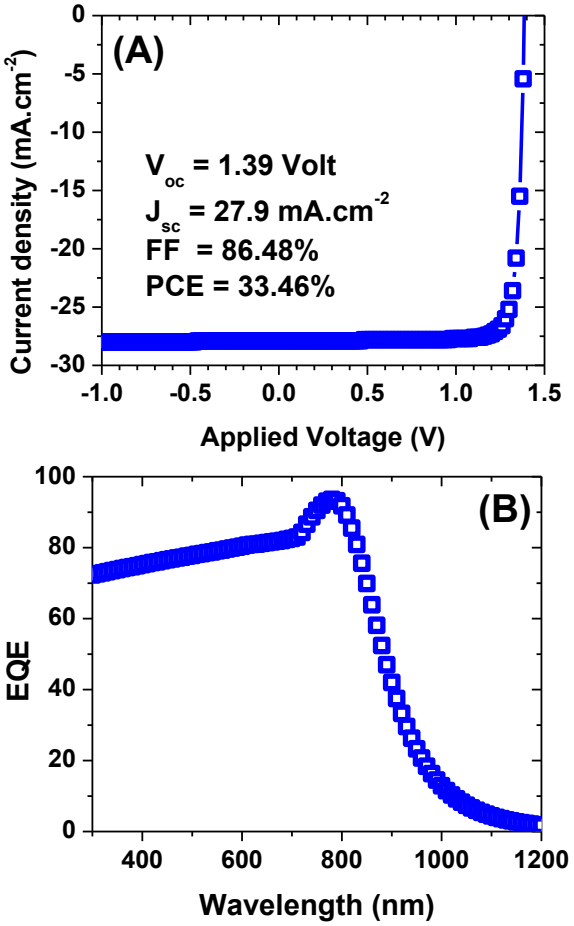

Fig. (11) (A) I-V characteristics and (B) the EQE spectra, of the optimum device

4. Conclusion

This study demonstrates the substantial benefits of incorporating a $CsGeI_2Br$ intrinsic perovskite layer into P3HT-based organic solar cells. By placing this layer between the P3HT donor and C60 acceptor materials, we achieved significant improvements in solar cell performance. Our results show that the perovskite layer enhances light absorption, improves charge carrier separation, and reduces recombination losses. These enhancements led to substantial increases in short-circuit current density, fill factor, and overall power conversion efficiency. Through simulation, we determined that optimizing several parameters of the perovskite layer, including thickness, bandgap, electron affinity, defect density, and effective density of states, significantly impacts device performance. The optimized configuration achieved a remarkable power conversion efficiency of 33.46%, far exceeding the efficiency of the baseline device without the perovskite interlayer. These findings highlight that lead-free perovskites such as $CsGeI_2Br$ offer a promising path toward developing more efficient solar cells while avoiding the environmental hazards associated with lead-based alternatives. We recommend further experimental validation and material engineering to develop these solar cells into scalable, efficient, and environmentally friendly energy solutions.

References

[1] Kenfack, A.D.K., Thantsha, N.M. and Msimanga, M., August. Simulation of lead-free heterojunction CsGeI2Br/CsGeI3-based perovskite solar cell using SCAPS-1D. In *Solar* 3(3)(2023): 458-472. MDPI.

[2] Kapim, K.A.D.; Konga, E.; Pelap, F.B. *Contribution of a non-uniform magnetic field on the electric power of a photovoltaic panel. J. Energy Technol. Policy*, 10(2020), 16–29

[3] Wang, Z., Bo, Y., Bai, P., Zhang, S., Li, G., Wan, X., Liu, Y., Ma, R. and Chen, Y., Self-sustaining personal all-day thermoregulatory clothing using only sunlight. *Science*, *382*(6676) (2023): 1291-1296.

[4] Li, S., Gao, M., Zhou, K., Li, X., Xian, K., Zhao, W., Chen, Y., He, C. and Ye, L., Achieving record- high stretchability and mechanical stability in organic photovoltaic blends with a dilute- absorber strategy. *Advanced Materials*, *36*(8)(2024): 2307278.

[5] Zhang, J., Mao, H., Zhou, K., Zhang, L., Luo, D., Wang, P., Ye, L. and Chen, Y., Polymer-Entangled Spontaneous Pseudo- Planar Heterojunction for Constructing Efficient Flexible Organic Solar Cells. *Advanced Materials*, *36*(7) (2024): 2309379.

[6] Lee, J.W., Seo, S., Lee, S.W., Kim, G.U., Han, S., Phan, T.N.L., Lee, S., Li, S., Kim, T.S., Lee, J.Y. and Kim, B.J., Intrinsically stretchable, highly efficient organic solar cells enabled by polymer donors featuring hydrogen- bonding spacers. *Advanced Materials*, *34*(50)(2022):2207544.

[7] Sun, S., Zha, W., Tian, C., Wei, Z., Luo, Q., Ma, C.Q., Liu, W. and Zhu, X., Solution processed semi- transparent organic solar cells over 50% visible transmittance enabled by silver nanowire electrode with sandwich structure. *Advanced materials*, *35*(46)(2023):2305092.

[8] Kadem, B., Alfahed, R.F., Al-Asadi, A.S. and Badran, H.A., Morphological, structural, optical, and photovoltaic cell of copolymer P3HT: ICBA and P3HT: PCBM. *Optik*, *204* (2020): 64153.

[9] Kadem, B.Y., Al-hashimi, M.K. and Hassan, A.K., The effect of solution processing on the power conversion efficiency of P3HT-based organic solar cells. *Energy Procedia*, *50* (2014): 237-245.

[10] Jeong, M., Choi, I.W., Go, E.M., Cho, Y., Kim, M., Lee, B., Jeong, S., Jo, Y., Choi, H.W., Lee, J. and Bae, J.H., Stable perovskite solar cells with efficiency exceeding 24.8% and 0.3-V voltage loss. *Science*, *369*(6511)(2020): 1615-1620.

[11] Momblona, C., Malinkiewicz, O., Roldán-Carmona, C., Soriano, A., Gil-Escrig, L., Bandiello, E., Scheepers, M., Edri, E. and Bolink, H.J., Efficient methylammonium lead iodide perovskite solar cells with active layers from 300 to 900 nm. *Apl Materials*, *2*(8)(2014).

[12] Wang, G.T., Wei, J.H. and Peng, Y.F., Electronic and optical properties of mixed perovskites CsSnxPb (1− x) I3. *AIP Advances*, *6*(6)(2016).

[13] Manspeaker, C. and Zakhidov, A., Predicting hybrid perovskite performance based on secondary cation choice. *Solar Energy*, *241*(2022): 686-692.

[14] Mahapatra, B., Krishna, R.V. and Patel, P.K., Design and optimization of CuSCN/CH3NH3PbI3/TiO2 perovskite solar cell for efficient performance. *Optics Communications*, *504*(2022): 127496.

[15] Kumar, R. and Chand, F., Performance enhancement in MA0. 7FA0. 3PbI3 based perovskite solar cell by gradient doping. *Optik*, *274*(2023): 170558.

[16] Ahmed, T., Shamim, S.U.D., Maity, S.K. and Basak, A., Performance evaluation of lead free CH3NH3SnI3/GeTe Tandem solar cell with HTL layer by SCAPS 1D. *Optik*, *282*(2023): 170836.

[17] Akhtarianfar, S.F., Shojaei, S. and Asl, S.K., High-performance CsPbI3/XPbI3 (X= MA and FA) heterojunction perovskite solar cell. *Optics Communications*, *512*(2022): 128053.

[18] Sk, M. and Ghosh, S., 16.35% efficient Cs2GeSnCl6 based heterojunction solar cell with hole-blocking SnO2 layer: DFT and SCAPS-1D simulation. *Optik*, *267*(2022): 169608.

[19] Ramachandran, K., Understanding the electronic, structural, optical, photovoltaic and thermoelectric properties of Cs2GeSnBr6 by first-principles and SCAPS-1D simulation. *Optik*, *282*(2023): 170822.

[20] Khatoon, S., Yadav, S.K., Chakraborty, V., Singh, J. and Singh, R.B., (2023). A simulation study of all inorganic lead-free CsSnBr3 tin halide perovskite solar cell. *Materials Today: Proceedings*.

[21] Sarkar, J., Talukdar, A., Debnath, P. and Chatterjee, S., Study of bromine substitution on band gap broadening with consequent blue shift in optical properties and efficiency optimization of lead-free CsGeI X Br3− X based perovskite solar cells. *Journal of Computational Electronics*, *22*(4)(2023): 1075-1088.

[22] Zhao, Y.Q., Wang, X., Liu, B., Yu, Z.L., He, P.B., Wan, Q., Cai, M.Q. and Yu, H.L., Geometric structure and photovoltaic properties of mixed halide germanium perovskites from theoretical view. *Organic Electronics*, 53(2018):50-56.

[23] Chiara, R., Morana, M., and Malavasi, L., *Germanium‐based halide perovskites: materials, properties, and applications. ChemPlusChem*, 86(6)(2021):879–888

[24] Xu, C., Zhang, Y., Luo, P., Sun, J., Wang, H., Lu, Y.W., Ding, F., Zhang, C. and Hu, J., Comparative study on TiO2 and C60 electron transport layers for efficient perovskite solar cells. *ACS Applied Energy Materials*, *4*(6)(2021): 5543-5553.

[25] Kadem, B.Y., Kadhim, R.G. and Banimuslem, H., Efficient P3HT: SWCNTs hybrids as hole transport layer in P3HT: PCBM organic solar cells. *Journal of Materials Science: Materials in Electronics*, *29*(11)(2018): 9418-9426.

[26] Roy, A. and Majumdar, A., Numerical optimization of Cu2O as HTM in lead-free perovskite solar cells: a study to improve device efficiency. *Journal of Electronic Materials*, 52(3)(2023):2020-2033.

[27] Mkawi, E.M., Al-Hadeethi, Y., Arkook, B. and Bekyarova, E., Doping with Niobium Nanoparticles as an Approach to Increase the Power Conversion Efficiency of P3HT: PCBM Polymer Solar Cells. *Materials*, 16(6)(2023): 2218.

[28] Chang, T.W., Tseng, C.C., Chen, D.W., Wu, G., Yang, C.L. and Chen, L.C., Preparation and characterization of thin-film solar cells with Ag/C60/MAPbI3/CZTSe/Mo/FTO multilayered structures. *Molecules*, 26(12) (2021): 3516.

[29] Peng, C.H. and Lin, Y.C., SCAPS-1D Simulation of Various Hole Transport Layers' Impact on CsPbI2Br Perovskite Solar Cells Under Indoor Low-Light Conditions. *Solids*, 6(3)(2025): 31.

[30] Arayro, J., Mezher, R. and Sabbah, H., Comparative simulation study of the performance of conventional and inverted hybrid tin-based perovskite solar cells. *Coatings*, *13*(7)92023): 1258.

[31] Mandadapu, U., Vedanayakam, S.V. and Thyagarajan, K., Simulation and analysis of lead based perovskite solar cell using SCAPS-1D. *Indian J. Sci. Technol*, *10*(1)(2017): 1-8.

[32] Kadem, B. Y., Kadhim, R. G., & Banimuslem, H., Efficient P3HT: SWCNTs hybrids as hole transport layer in P3HT: PCBM organic solar cells. J*ournal of Materials Science: Materials in Electronics*, 29(11)(2018): 9418-9426.

[33] Son, D.H., Park, H.K., Kim, D.H., Kang, J.K., Sung, S.J., Hwang, D.K., Lee, J., Jeon, D.H., Cho, Y., Jo, W. and Lee, T., Vertical plane depth-resolved surface potential and carrier separation characteristics in flexible CZTSSe solar cells with over 12% efficiency. *Carbon Energy*, *6*(3)(2024): e434.

[34] Kirchartz, T., Gong, W., Hawks, S.A., Agostinelli, T., MacKenzie, R.C., Yang, Y. and Nelson, J., Sensitivity of the Mott–Schottky

analysis in organic solar cells. *The Journal of Physical Chemistry C*, *116*(14)(2012):7672-7680.

[35] Bisquert, J., Garcia-Belmonte, G., Munar, A., Sessolo, M., Soriano, A. and Bolink, H.J., Band unpinning and photovoltaic model for P3HT: PCBM organic bulk heterojunctions under illumination. *Chemical Physics Letters*, *465*(1-3)(2008):57-62.

[36] Chouhan, A.S., Jasti, N.P. and Avasthi, S., Effect of interface defect density on performance of perovskite solar cell: Correlation of simulation and experiment. *Materials Letters*, *221(2018)*: 150-153.

[37] Kanoun, A.A., Kanoun, M.B., Merad, A.E. and Goumri-Said, S., Toward development of high-performance perovskite solar cells based on CH3NH3GeI3 using computational approach. *Solar Energy*, *182*(2019): 237-244.

[38] Ouslimane, T., Et-Taya, L., Elmaimouni, L. and Benami, A., Impact of absorber layer thickness, defect density, and operating temperature on the performance of MAPbI3 solar cells based on ZnO electron transporting material. *Heliyon*, *7*(3)(2021).

[39] Kadem, B., Cranton, W. and Hassan, A., Metal salt modified PEDOT: PSS as anode buffer layer and its effect on power conversion efficiency of organic solar cells. *Organic Electronics*, *24*(2015): 73-79.

[40] Kadem, B.Y. and Abbas, E.M., Optimization of Several Parameters Towards 30% Efficiency Perovskite Based Solar Cell Using SCAPS-1D Software. *Iraqi Journal of Physics*, *22*(4)(2024): 117-129.

[41] Lee, H.W., Biswas, S., Lee, Y. and Kim, H., Over 23% Efficiency Under Indoor Light in Gallium-Doped Zinc Oxide Electron-Transport-Layer-Based Inverted Organic Solar Cell to Power IoT Devices. *IEEE Internet of Things Journal*, *10*(18)(2023):15923-15930.

[42] Al-hashimi, M.K., Kadem, B.Y. and Hassan, A.K., Rutile TiO2 films as electron transport layer in inverted organic solar cell. *Journal of Materials Science: Materials in Electronics*, *29*(9)(2018):7152-7160.

[43] Miah, M.H., Khandaker, M.U., Rahman, M.B., Nur-E-Alam, M. and Islam, M.A., Band gap tuning of perovskite solar cells for enhancing the efficiency and stability: issues and prospects. *RSC advances*, *14*(23)(2024): 15876-15906.

[44] Eperon, G.E., Stranks, S.D., Menelaou, C., Johnston, M.B., Herz, L.M. and Snaith, H.J., Formamidinium lead trihalide: a broadly tunable perovskite for efficient planar heterojunction solar cells. *Energy & environmental science*, *7*(3)(2014): 982-988.

[45] Son, D.Y., Lee, J.W., Choi, Y.J., Jang, I.H., Lee, S., Yoo, P.J., Shin, H., Ahn, N., Choi, M., Kim, D. and Park, N.G., Self-formed grain boundary healing layer for highly efficient CH3NH3PbI3 perovskite solar cells. *Nature Energy*, *1*(7)(2016): 1-8.

[46] Edoff, M., Jarmar, T., Nilsson, N.S., Wallin, E., Högström, D., Stolt, O., Lundberg, O., Shafarman, W. and Stolt, L., High V oc in (Cu, Ag)(In, Ga) Se 2 Solar Cells. *IEEE Journal of Photovoltaics*, *7*(6)(2017):1789-1794.

[47] Wolff, C.M., Caprioglio, P., Stolterfoht, M. and Neher, D., Nonradiative recombination in perovskite solar cells: the role of interfaces. *Advanced Materials*, *31*(52)(2019):1902762.

[48] Wang, K., Liu, C., Du, P., Zheng, J. and Gong, X., Bulk heterojunction perovskite hybrid solar cells with large fill factor. *Energy & Environmental Science*, *8*(4)(2015): 1245-1255.

[49] Ding, C., Zhang, Y., Liu, F., Kitabatake, Y., Hayase, S., Toyoda, T., Yoshino, K., Minemoto, T., Katayama, K. and Shen, Q., Effect of the conduction band offset on interfacial recombination behavior of the planar perovskite solar cells. *Nano Energy*, *53(2018):*17-26.

[50] Bagade, S.S., Barik, S.B., Malik, M.M. and Patel, P.K., (2023). Impact of band alignment at interfaces in perovskite-based solar cell devices. *Materials Today: Proceedings*.

[51] Tan, K., Lin, P., Wang, G., Liu, Y., Xu, Z. and Lin, Y., Controllable design of solid-state perovskite solar cells by SCAPS device simulation. *Solid-State Electronics*, *126*(2016):75-80.

[52] Du, H.J., Wang, W.C. and Zhu, J.Z., Device simulation of lead-free CH3NH3SnI3 perovskite solar cells with high efficiency. *Chinese Physics B*, *25*(10)(2016):108802.

[53] Bansal, S. and Aryal, P., (2016), June. Evaluation of new materials for electron and hole transport layers in perovskite-based solar cells through SCAPS-1D simulations. In *2016 IEEE 43rd photovoltaic specialists conference (PVSC)* (pp. 0747-0750). IEEE.

[54] Siekmann, J., Ravishankar, S. and Kirchartz, T., Apparent defect densities in halide perovskite thin films and single crystals. *ACS Energy Letters*, *6*(9)(2021): 3244-3251.

[55] Kang, J. and Wang, L.W., High defect tolerance in lead halide perovskite CsPbBr3. *The journal of physical chemistry letters*, *8*(2)(2017):489-493.

[56] Chowdhury, M.S., Shahahmadi, S.A., Chelvanathan, P., Tiong, S.K., Amin, N., Techato, K.A., Nuthammachot, N., Chowdhury, T. and Suklueng, M., Effect of deep-level defect density of the absorber layer and n/i interface in perovskite solar cells by SCAPS-1D. *Results in Physics*, 16(2020):102839.

[57] Dai, J., Tang, W., Li, T., Xu, C., Zhao, M., Ji, P., Li, X., Zhang, F., Cai, H. and Wu, X., First-Principles Study of Halide Modulation on Deep-Level Traps in FAPbI3. Nanomaterials, 15(13)(2025): 981.
[58] Hossain, E.S., Chelvanathan, P., Shahahmadi, S.A., Sopian, K., Bais, B. and Amin, N., Performance assessment of Cu2SnS3 (CTS) based thin film solar cells by AMPS-1D. *Current Applied Physics*, *18*(1)(2018): 79-89.
[59] Kirchartz, T. and Rau, U., Linking structural properties with functionality in solar cell materials–the effective mass and effective density of states. *Sustainable Energy & Fuels*, *2*(7)(2018): 1550-1560.
[60] Zhou, Y. and Long, G., Low density of conduction and valence band states contribute to the high open-circuit voltage in perovskite solar cells. *The Journal of Physical Chemistry C*, *121*(3)(2017):1455-1462.
[61] Bartesaghi, D., Pérez, I.D.C., Kniepert, J., Roland, S., Turbiez, M., Neher, D. and Koster, L.J.A., Competition between recombination and extraction of free charges determines the fill factor of organic solar cells. *Nature communications*, *6*(1)(2015):7083.

Table (1) The parameters used in SCAPS-1D software to evaluate the device performance

Parameters	P3HT [1]	$CsGeI_2Br$ [1]	C60 [30]	Cu_2O [30]	PCBM [31]
Thickness (nm)	100	Variable (50-500)	100	50	50
Band gap (eV)	1.7	Variable (1.5-1.6)	1.7	2.17	2.1
Electron affinity (eV)	3.5	Variable (3.5-4)	3.9	3.2	3.9
Dielectric permittivity	3	18	4.2	7.11	3.9
CB effective DOS ($1/cm^3$)	2.2×10^{18}	Variable (1×10^{16} -1×10^{19})	8×10^{19}	2.02×10^{17}	2.2×10^{19}
VB effective DOS ($1/cm^3$)	2.2×10^{18}	Variable (1×10^{16} -1×10^{19})	1×10^{20}	1.1×10^{19}	2.2×10^{19}
Electron thermal velocity (cm/s)	1×10^{7}	1×10^{7}	1×10^{7}	1×10^{7}	1×10^{7}
Hole thermal velocity (cm/s)	1×10^{7}	1×10^{7}	1×10^{7}	1×10^{7}	1×10^{7}
Hole mobility ($cm^2/V.s$)	1.8×10^{-2}	20	8×10^{-2}	80	0.001
Electron mobility ($cm^2/V.s$)	1.8×10^{-3}	20	50	20	0.002
N_D ($1/cm^3$)	0	1×10^{16}	1×10^{17}	-	1×10^{19}
N_A ($1/cm^3$)	1×10^{18}	1×10^{16}	0	1×10^{18}	-
Defect energetic distribution	Single	Neutral	Single	Neutral	Neutral
Defect density (N_t) ($1/cm^3$)	1×10^{14}	Variable (1×10^{16} -1×10^{17})	1×10^{16}	1×10^{14}	1×10^{18}

Table (3) The optimum parameters used in SCAPS-1D to evaluate the best device performance

Parameters	P3HT	$CsGeI_2Br$ (Initial parameters)	$CsGeI_2Br$ (optimum parameters)	C60	Cu_2O	PCBM
Thickness (nm)	100	500	500	100	50	50
Band gap (eV)	1.7	1.579	1.58	1.7	2.17	2.1
Electron affinity (eV)	3.5	3.79	4	3.9	3.2	3.9
Dielectric permittivity	3	18	18	4.2	7.11	3.9
CB effective DOS ($1/cm^3$)	2.2×10^{18}	9.65×10^{17}	1×10^{17}	8×10^{19}	2.02×10^{17}	2.2×10^{19}
VB effective DOS ($1/cm^3$)	2.2×10^{18}	1.04×10^{18}	1×10^{17}	1×10^{20}	1.1×10^{19}	2.2×10^{19}
Electron thermal velocity (cm/s)	1×10^{7}	1×10^{7}	1×10^{7}	1×10^{7}	1×10^{7}	1×10^{7}
Electron thermal velocity (cm/s)	1×10^{7}	1×10^{7}	1×10^{7}	1×10^{7}	1×10^{7}	1×10^{7}
Hole mobility ($cm^2/V.s$)	1.8×10^{-2}	20	20	8×10^{-2}	80	0.001
Electron mobility ($cm^2/V.s$)	1.8×10^{-3}	20	20	50	20	0.002
N_D ($1/cm^3$)	0	1×10^{16}	1×10^{16}	1×10^{17}	-	1×10^{19}
N_A ($1/cm^3$)	1×10^{18}	1×10^{16}	1×10^{16}	0	1×10^{18}	-
Defect energetic distribution	Single	Neutral	Neutral	Single	Neutral	Neutral
Defect density (N_t) ($1/cm^3$)	1×10^{14}	1×10^{16}	1×10^{16}	1×10^{16}	1×10^{14}	1×10^{18}

